RSC Advances

PAPER

View Article Online
View Journal | View Issue

Cite this: *RSC Adv.*, 2024, **14**, 8526

Preparation of Co–Ni–Ce/TiC alloy coatings by double-pulse under a sulfamic acid system and a process mechanism study

Jidong Li,[a] Hongxuan Xing,[a] Senhu Jin,[a] Yaowu Wang *[b] and Jinlin Lu[c]

To enhance the protective ability of copper crystallizers and extend their service life, this study explores the use of double pulse co-deposition under a sulfamic acid system to create protective coatings such as Co–Ni. The hardness test and friction wear analysis compare Co–Ni, Co–Ni–Ce, and Co–Ni–Ce/TiC coatings, revealing that the Co–Ni–Ce/TiC coating exhibits the most outstanding protective performance. SEM and XRD techniques are employed to characterize the three protective coatings, demonstrating that the incorporation of rare-earth cerium and nanoparticles improves the coating morphology and modifies their crystalline phase structure. Furthermore, cyclic voltammetry tests on the plating solutions of the three protective coatings indicate that the addition of Ce^{3+} and nanoparticles influences the deposition potentials. The deposition of Co^{2+} and Ni^{2+} follows a two-step, two-electron process, while the deposition of Ce^{3+} follows a one-step, three-electron process. It is observed that the deposition of all three ions is irreversible. To gain further insights into the nucleation mechanism of Ce^{3+}, a chronoamperometry test is conducted, revealing that the nucleation of Ce^{3+} is a transient process controlled by diffusion.

Received 4th February 2024
Accepted 8th March 2024

DOI: 10.1039/d4ra00896k

rsc.li/rsc-advances

1 Introduction

In the steel industry, the copper crystallizer plays a crucial role in the steelmaking process.[1] However, the harsh steelmaking environment can cause irreversible damage to the surface of the copper crystallizer, resulting in steel leakage over time and significant losses. To protect the copper crystallizer, manufacturers apply protective coatings on its surface.[2] The Co–Ni alloy is commonly used for its excellent wear resistance, corrosion resistance, and thermal stability, effectively extending the service life of the copper crystallizer.[3]

The most common method for applying protective coatings is electrodeposition, which traditionally utilizes direct current deposition technology. However, this approach has drawbacks such as ion concentration polarization and hydrogen precipitation reaction at the cathode interface during electrodeposition. These issues reduce current efficiency and can lead to irregular crystal growth and structural defects in the plating layer.[4] Double-pulse plating is a technique that utilizes reverse current to improve the plating process. It helps replenish metal ions near the specimen to be plated, reducing concentration polarization and enhancing the nucleation rate within the plating layer. This technique promotes the refinement of crystal grain.[5] Gao *et al.*[6] conducted a study where they prepared a Co–Ni/graphene composite coating on a copper crystallizer substrate. By adjusting the percentage of Co content in the coating, they found that high Co composite coatings exhibited excellent hardness and good wear resistance. Rare earth elements, with their unique atomic structure, are extensively utilized in various sectors such as electronics, machinery, energy, environmental protection, and agriculture. The addition of rare earth elements enhances the surface properties of coatings, impacting factors like deposition rate, surface morphology, wear resistance, and corrosion resistance.[7] Cerium (Ce) has emerged as a key element for studying the characteristics of rare earth elements. During the deposition process, Ce^{3+} can absorb coating defects, enhancing surface morphology and overall performance, thereby extending the lifespan of the workpiece.[8] Fu *et al.* conducted a study where they utilized the jet-electrodeposition method to prepare Ni–W–Ce alloy coatings. Their findings indicated that the inclusion of rare earth Ce significantly improved the hardness and wear resistance of the coatings.[7] Additionally, the presence of Ce in the coatings induced lattice distortion within the alloy coatings.[7] Another study by Li *et al.*[9] involved the preparation of Ni–Co/ZrO_2 composite coatings by adding nano-ZrO_2 in a sulfamic acid solution system. The addition of nano-ZrO_2 significantly improved the mechanical and chemical properties of the composite coatings, making the electrode reaction more likely to occur. Wang H[10] utilized the double pulse electrodeposition process to fabricate Ni–TiC composite coatings. The inclusion

[a]*School of Materials and Metallurgy, University of Science and Technology Liaoning, Anshan 114051, China*
[b]*Northeastern University, School of Metallurgy, Shenyang 110000, China*
[c]*Guangzhou Maritime University, Guangzhou 510725, China*

Table 1 Reagent concentration and process conditions

	Prerequisites	Co–Ni	Co–Ni–Ce	Co–Ni–Ce/TiC	Pure
Concentration (g L^{-1})	Ni $(SO_3NH_2)_2 \cdot 4H_2O$	100	100	100	AR
	Co $(SO_3NH_2)_2 \cdot 4H_2O$	33.3	33.3	33.3	AR
	$NiCl_2 \cdot 6H_2O$	16.6	16.6	16.6	AR
	H_3BO_3	30	30	30	AR
	$CeCl_3 \cdot 7H_2O$	—	2	2	AR
	$C_{12}H_{25}SO_4Na$	0.15	0.15	0.15	AR
	$C_6H_8O_7H_2O$	30	30	30	AR
	NH_4Cl	33	33	33	AR
	TiC (40 nm)	—	—	5	AR
Process parameters	Positive current density (A dm^{-2})	4	4	4	—
	Positive duty cycle (%)	40	40	40	—
	Positive pulse frequency (kHZ)	20	20	20	—
	Reversed current density (A dm^{-2})	0.2	0.2	0.2	—
	Reverse duty cycle (%)	40	40	40	
	Reverse pulse frequency (kHZ)	2	2	2	—
	pH	4	4	4	—
	T (°C)	40	40	40	—
	Time (min)	75	75	75	—

of nano TiC particles in the plating exhibited superior resistance to high temperatures compared to other particles. This characteristic makes it highly suitable for application on the surface of the copper crystallizer.

The double-pulse preparation of Co–Ni–Ce/TiC alloys has been scarcely reported. Consequently, this study presents the preparation of Co–Ni–Ce/TiC alloy coating through double-pulse one-step co-deposition on the copper crystallizer's surface. This approach eliminates the need for additives in previous DC electrodeposition and contributes to the lightweighting of equipment. Moreover, this paper not only investigates the process properties of the three alloys but also elucidates the mechanism of the ion deposition process. The combination of these two research aspects facilitates the advancement and exploration of surface functional alloy coatings, thereby expanding the range of applications for copper metal materials.

2 Materials and methods

2.1 Experimental materials

In the experiments, a 20 × 40 × 2 mm copper (Cu) plate was employed as the cathode, while a 5 × 10 × 50 mm nickel (Ni) plate was utilized as the anode, and the distance between the poles was set at 20 mm. The Table 1 provides information on the concentrations of reagents used during the process experiments, along with the corresponding conditions. The experimental concentration in this article is based on the experimental results obtained during multiple process explorations, and the process exploration process is not explained in this article.

2.2 Composite coating procedure

To prepare the surface for the deposition of Co–Ni–Ce/TiC, it underwent a polishing treatment using sandpaper of varying mesh sizes (400, 800, 1200, 1500, and 2000). Subsequently, the

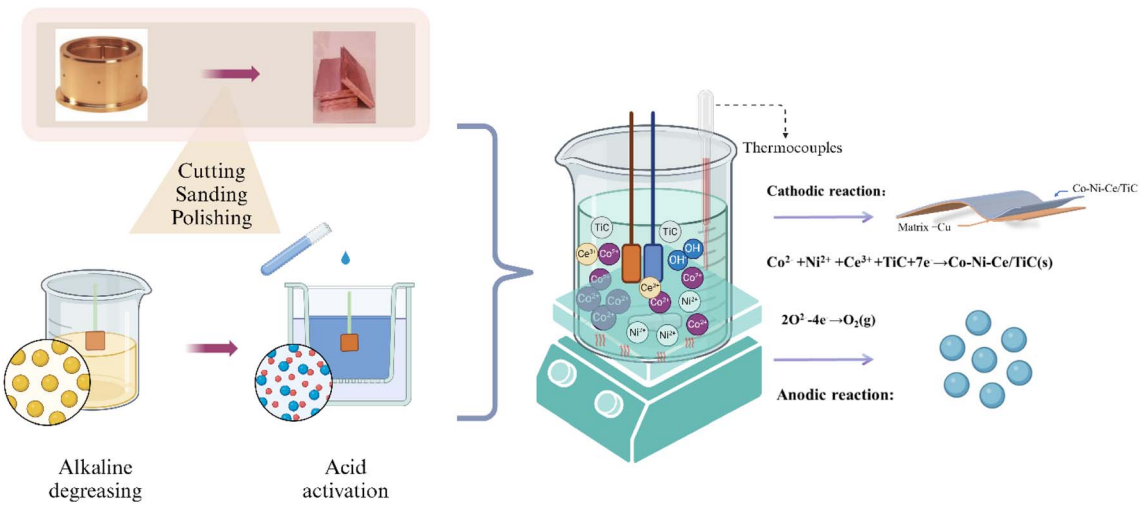

Fig. 1 Flow chart of Co–Ni–Ce/TiC alloy plating process preparation.

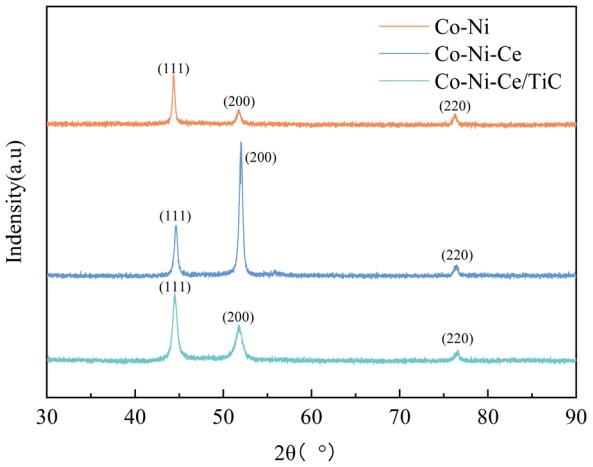

Fig. 2 XRD curves of three different coatings.

Cu surface was subjected to cleansing and activation using a 5% HCl solution to eliminate the surface film, thereby enhancing the bonding strength of the Co–Ni–Ce/TiC coating. Deionized water was used for rinsing purposes following the activation step. Ultimately, the electrodeposition process led to the formation of the Co–Ni–Ce/TiC alloy coating. The schematic representation of this entire sequence is illustrated in Fig. 1.

2.3 Surface characterization and mechanism test

To observe the surface morphology of the sample, a sigma500 scanning electron microscope (SEM) was utilized. Additionally, a Bruker energy dispersive spectrometer (EDS) was employed to analyze the coated sample's chemical composition and elemental distribution. X-ray diffraction (XRD) experiments were conducted on various coatings using an Ultam IV X-ray diffractometer manufactured by Rigaku, Japan. The X-ray tube used CuKα1 radiation with a wavelength (λ) of 0.15405 nm, a tube voltage of 40 kV, and a tube current of 20 mA. The scanning rate was set at 40° min^{-1}, with a scanning range (2θ) of 30° to 90°.

The hardness values of both the substrate and coating were examined using an HVS-5 micro-Vickers hardness tester. The force was applied at a speed of 0.05 mm s^{-1}, with a load force of 200 g, and a holding time of 10 s, and five replicates were averaged. The coated samples' abrasion resistance was evaluated using the MS-T3100 ball and disk friction and wear tester manufactured by Huahui Instrument Technology in Lanzhou. In this test, Si_3N_4 grinding balls with a diameter of 2 mm were employed, with an applied load of 400 g. The tester operated at a rotational speed of 200 r min^{-1}, with a radius of rotation of 4 mm, and a test time of 30 min.

For the mechanical experiment, we employed a copper coating with dimensions of 20 × 40 × 2 mm as the cathode. The anode, on the other hand, consisted of a platinum sheet measuring 10 × 20 × 0.5 mm. To compare electrochemical potentials, we utilized an Ag/AgCl electrode as the reference electrode. Maintaining uniformity, both the cathode-to-reference and anode-to-reference gaps were set at 20 mm. Oxygen is removed from the solution by passing argon gas before each test.

3 Results and discussion

3.1 Characterization of composite plating

3.1.1 XRD characterization. The diffraction peaks with 2θ of 44°, 52°, and 76° correspond to the (111), (200), and (220) directions of the space group *Fm3m* (225), respectively, and are consistent with the diffraction peaks of Ni (JCPDS#040850) and Co (JCPDS#150806), and together with the results in Fig. 2, it can be determined that the plating layer is a single-phase solid-solution alloy formed by Ni and Co.[11] The EDS data from Fig. 3 shows very little Ce and Ti, so the associated metal phases were not detected in the XRD. The lattice constants of alloys $a = 3.524$ Å, $b = 3.524$ Å, $c = 3.524$ Å, $\alpha = \beta = \gamma = 90°$ belong to the Face Centered Cubic.

In addition, both Co–Ni–Ce and Co–Ni–Ce/TiC alloys show enhancement of the diffraction peaks at (200) compared to Co–Ni alloys, and the enhancement is most obvious for Co–Ni–Ce alloys, which may be due to the fact that rare earth elements have large atomic radii and high ionic valence, and the addition of Ce affects the grain growth direction of Co–Ni alloys which would cause it to develop more towards the (200) crystal plane, and the addition of TiC would equalize this effect.[7,10,12]

By observing the XRD, it can be found that there is a small broadening of the peak shape, indicating that the addition of Ce and TiC can effectively inhibit the growth of grains and make the plated layer fine grains. To further obtain the grain size, the Debye–Scherrer eqn (1) (ref. 7) was used for the calculation.

$$D = K\lambda/\beta \cos\theta \quad (1)$$

where K is Scherrer's constant, taken as 0.89, λ is the X-ray diffraction wavelength, 0.15405 nm; β is the half-height width

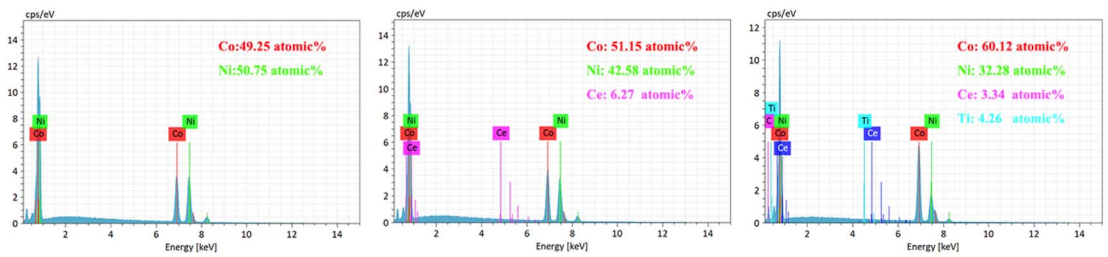

Fig. 3 EDS chaaracterization of three different coatings.

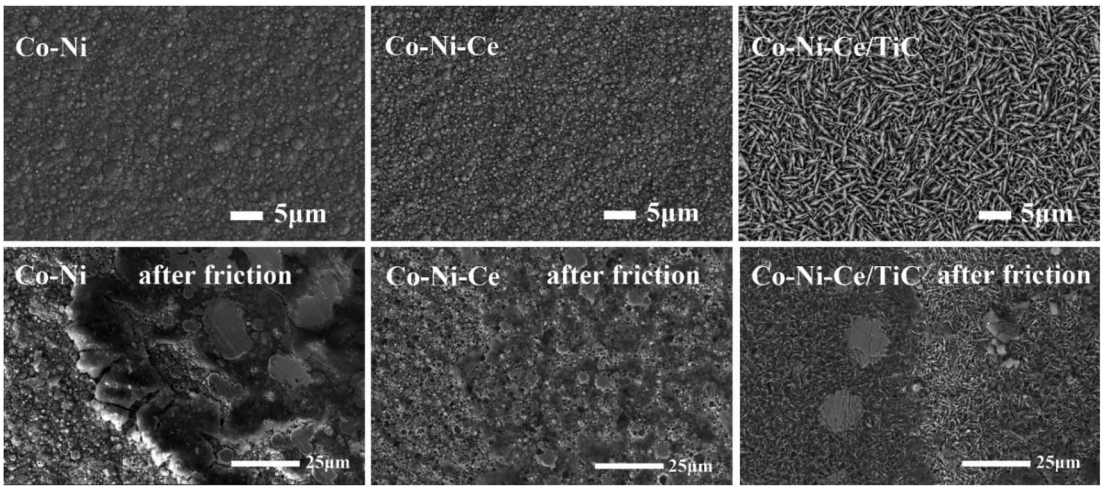

Fig. 4 SEM characterization of three samples before friction.

of the diffraction peaks of the samples; θ is the diffraction angle. The average grain size of the Co–Ni alloy coating was calculated to be 54.7 nm. According to the eqn (1), the average grain size of the Co–Ni–Ce alloy was calculated to be 53.6 nm, and the average grain size of the Co–Ni–Ce/TiC composite coating was 50.6 nm.

3.1.2 EDS characterization. The adsorption of rare earth ions on the substrate surface promotes the adsorption of metal ions and facilitates the subsequent processes of adsorption, discharge, reduction, and deposition, ultimately leading to the formation of alloy coatings containing rare earths. The results presented in Fig. 3 demonstrate that the incorporation of rare earth cerium and nanoparticle TiC results in an increase in Co content and a decrease in Ni content. This phenomenon can be attributed to the unique ability of rare earth metal ions to selectively adsorb onto the electrode interface, thereby altering the electron layer structure of the interface.[13] This alteration impedes the deposition of Ni and the diffusion process at the interface, making it more challenging for Ni to deposit.[13] Additionally, the high specific surface area of TiC nanoparticles enhances the activity of the Co–Ni alloy surface, thereby influencing the adsorption and diffusion processes of Co and Ni.[14] The Co–Ni alloy is classified as an anomalous co-deposition process, where the increase in active sites enhances the formation of Co $(OH)_2$ on the cathode surface. Scholars have noted that Co $(OH)_2$ hinders the deposition of Ni while aiding in the deposition of Co.[15,16]

3.1.3 SEM characterization. Fig. 4 demonstrates the SEM characterization of Co–Ni plating with the addition of metal Ce and TiC. The microscopic morphology of the Co–Ni–Ce ternary alloy coating shows that the addition of Ce improves the surface quality of the coating. This improvement is attributed to the addition of moderate amounts of rare earth Ce elements and complexing agents, which enhance the cathodic polarization and refine the grain size of the coating.[17] Compared to the Co–Ni alloy coating, the Co–Ni–Ce alloy coating exhibits less plastic deformation and only a small portion of flat surfaces due to friction. This suggests that the addition of Ce improves the coating's hardness by refining the grains.[18] Furthermore, the addition of TiC nanoparticles allows TiC to form a strong metallurgical bond with Co–Ni–Ce. Friction and wear tests reveal that this bond provides better strength and interfacial compatibility, thereby increasing the robustness and wear resistance of the plating. It also effectively hinders contact and wear between the friction surfaces.[19] In conclusion, the surface of the Co–Ni–Ce/TiC composite plating is slightly superior to that of the Co–Ni–Ce alloy plating. After frictional wear, it exhibits a lubricated surface morphology, with the wear-resistant nanomaterial TiC playing a lubricating role.

As illustrated in Fig. 5, the Co–Ni, Co–Ni–Ce, Co–Ni–Ce/TiC, and Cu exhibit a two-layer composite structure. The Co–Ni layer has a thickness of 300 μm, the Co–Ni–Ce layer has a thickness of 250 μm, and the Co–Ni–Ce/TiC layer has a thickness of 150 μm, all of which can be regulated by the deposition time during actual production. The reduction in layer thickness following the addition of Ce and TiC is attributed to the decrease in deposition potential caused by these substances, resulting in slower deposition and finer layers.[7,14] This decrease in

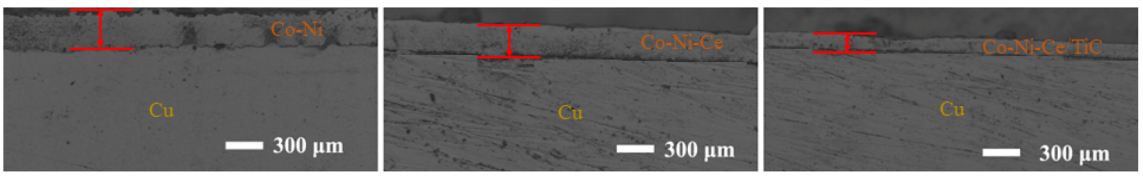

Fig. 5 Cross-sectional SEM characterisation of three samples.

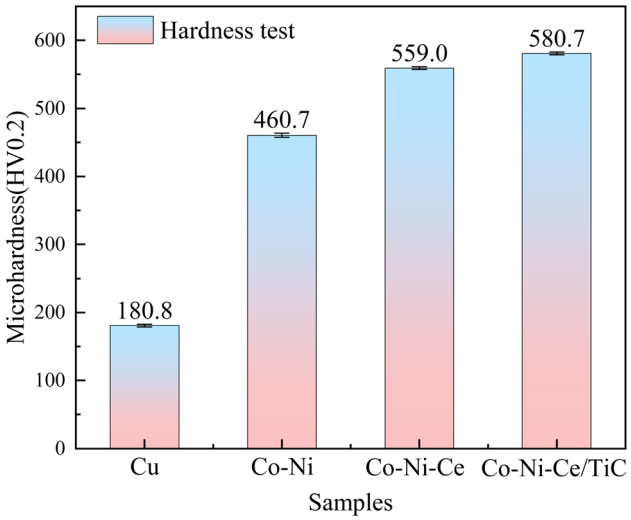

Fig. 6 Hardness test graph of different samples.

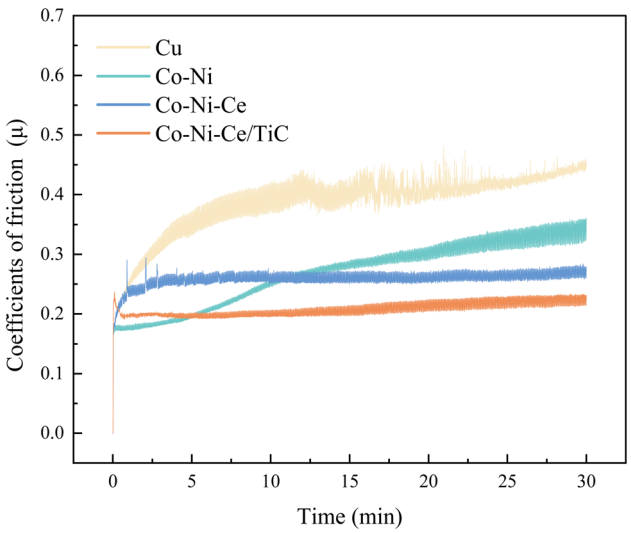

Fig. 7 Time variation curve of friction coefficient of samples.

deposition potential is also confirmed through subsequent cyclic voltammetry analysis.

3.2 Performance testing

3.2.1 Hardness test. According to Fig. 6, the Co–Ni alloy has the ability to significantly enhance the hardness of the Cu matrix. This results in the protection of the crystallizer surface against friction damage and extends the service life of the copper crystallizer. The addition of rare earth Ce increases the hardness of the Co–Ni alloy to 559.0 HV0.2. The introduction of rare earth Ce brings about changes in the crystal structure, leading to distortions, strains, and the formation of dislocations and solid solutions within the crystal.[3] This complexity in the crystal structure contributes to the increased hardness of the alloy. Furthermore, the addition of nanoparticle TiC reduces the grain size and increases the grain boundary area.[10] This impedes the movement of dislocations and slip of the crystals, thereby further enhancing the hardness of the alloy.

3.2.2 Friction wear test. As depicted in Fig. 7, the friction coefficients of the Co–Ni–Ce/TiC composite coating and the Co–Ni–Ce alloy coating remain stable throughout the friction and wear experiments. On the other hand, the friction coefficients of the Co–Ni alloy coating have been observed to increase during these experiments. This can be attributed to the fact that the Co–Ni–Ce alloy coating, unlike the Co–Ni alloy coating, exhibits a lower and relatively smooth friction coefficient. This improvement is achieved by incorporating rare earth Ce, which enhances the surface denseness and internal structure of the coating.[7] Furthermore, the Co–Ni–Ce/TiC composite coating demonstrates the lowest and most stable friction coefficient. This is attributed to the addition of wear-resistant TiC nanoparticles, which effectively prevent bonding between the friction partner and the coating surface.[10]

The average friction coefficient of the Co–Ni alloy coating is 0.2693, and the wear rate is 1.99×10^{-5} g m^{-1}. According to Table 2, the average friction coefficient of the Co–Ni–Ce alloy coating is 0.2582, and the wear rate is 1.72×10^{-5} g m^{-1}. The average friction coefficient of the Co–Ni–Ce/TiC composite coating is 0.2079, and the wear rate is 1.06×10^{-5} g m^{-1}, and the wear-resistant properties are all better than those of the Co–Ni–Ce alloy plating.

3.3 Mechanism of the electrode reaction

3.3.1 Cyclic voltammetry analysis. To investigate the effect of Ce^{3+} on the deposition potential of the Co–Ni system plating solution and the effect of TiC on the deposition potential of the Co–Ni–Ce system plating solution. Cyclic voltammetry (CV) tests were carried out under the three systems with scanning potentials ranging from −1.6 V to 0.7 V and a sweep rate of 60 mV s^{-1}. The results are shown in Fig. 8.

Table 2 Friction and wear data of Co–Ni–Ce/TiC coatings

	Cu	Co–Ni	Co–Ni–Ce	Co–Ni–Ce/TiC
Coefficient of friction-μ_{max}	0.4807	0.3603	0.2947	0.2373
Average coefficient of friction-$\bar{\mu}$	0.3863	0.2693	0.2582	0.2079
Friction-F_{max}/N	1.8844	1.4123	1.1551	0.9304
Average friction-F/N	1.5142	1.0555	1.0120	0.8145
Abrasion quantity-ΔM/mg	5.0	1.5	1.3	0.8
Wear rate-W/g m^{-1}	6.63×10^{-5}	1.99×10^{-5}	1.72×10^{-5}	1.06×10^{-5}

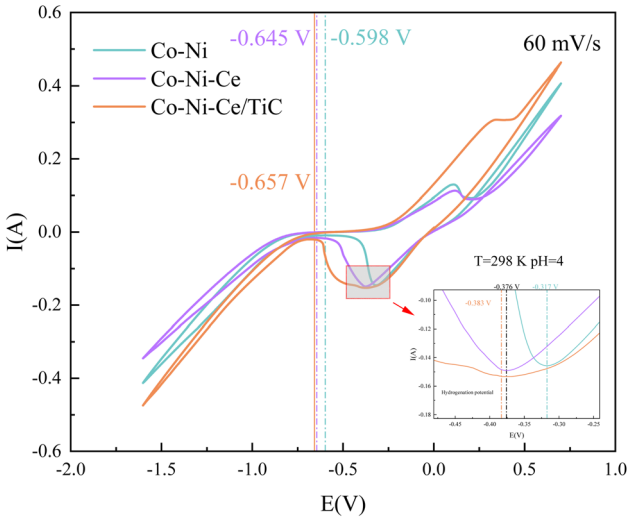

Fig. 8 Cyclic voltammetric testing in three systems.

As can be seen in Fig. 8, the test curves at different sweep speeds in the negative direction scanning showed a reduction peak within the scanning potential of −0.25 V to −0.5 V. This peak is the reduction peak of H^+, and the reduction reaction formula is: $2H_2O + 2e^- \rightarrow H_2\uparrow + 2OH^-$.[20] In addition to this, Co^{2+} and Ni^{2+} each gain one electron and combine with OH^- to become $CoOH_{ads}$ and $NiOH_{ads}$.[15,16] The current density started to increase in the scanning potential interval from −0.65 V to −0.75 V. This interval potential is the starting potential for the co-deposition of the alloy.[21] During the forward scan of the CV test, an oxidation peak in the potential range of 0.1 V to 0.5 V appeared, which was caused by the anodic dissolution of the electrode surface.[20]

By comparing the CV curves of the three systems, it was observed that the reduction potential for hydrogen precipitation and the reduction potential for metal co-deposition in the Co–Ni–Ce system were negatively shifted compared to the Co–Ni system. This suggests that the addition of Ce^{3+} increased the cathodic polarization of the system solution and hindered the reduction reaction in the Co–Ni system, but promoted the induced co-deposition of Ce^{3+} with Co–Ni.[22] The negative shift of the co-deposition potential of TiC nanoparticles relative to that of Co–Ni–Ce is not significant, indicating that the addition of nanoparticles has less influence on the deposition effect potential in this system.[23] Additionally, when conducting the cyclic voltammetry test with a positive sweep, it was noticed that the potential of the oxidation peak in the CV became more positive with the addition of TiC nanoparticles. This suggests that the Co–Ni–Ce/TiC composite plating layer exhibits greater resistance to oxidation.[23] To gain further insights into the deposition mechanism of the ions and the related electrochemical parameters, CV and chronoamperometry tests were conducted at different sweep speeds for the Co–Ni–Ce system.

From Fig. 9(a), it can be observed that as the sweep speed increases, the reduction peak potential shifts towards the negative direction and the reduction peak current gradually increases. Similarly, the oxidation peak potential shifts towards the positive direction and the oxidation peak current also gradually increases. To further confirm the number of electrons transferred by ions during the deposition process, four data points were selected at the reduction peak A and at the co-deposition potential B for fitting at a sweep speed of 60 mV s^{-1}. The relevant data calculations were recorded in Table 3, and the electron transfer number was calculated using the Nernst equation.[21]

$$E = Y + \frac{1.857RT\lg[(I - I_p)/I]}{nF} \quad (2)$$

As can be seen in Fig. 10, the fitting coefficients are 0.998 and 0.976, indicating a good linear relationship of the point data. Based on the fitting slopes in Fig. 10, the number of transferred electrons of the ions can be calculated as follows:[21]

$$\begin{cases} n = \dfrac{1.857 \times 8.314 \times 298}{96500 \times 0.046} = 1.01 \approx 1 \\ n = \dfrac{1.857 \times 8.314 \times 298}{96500 \times 0.014} = 3.33 \approx 3 \end{cases}$$

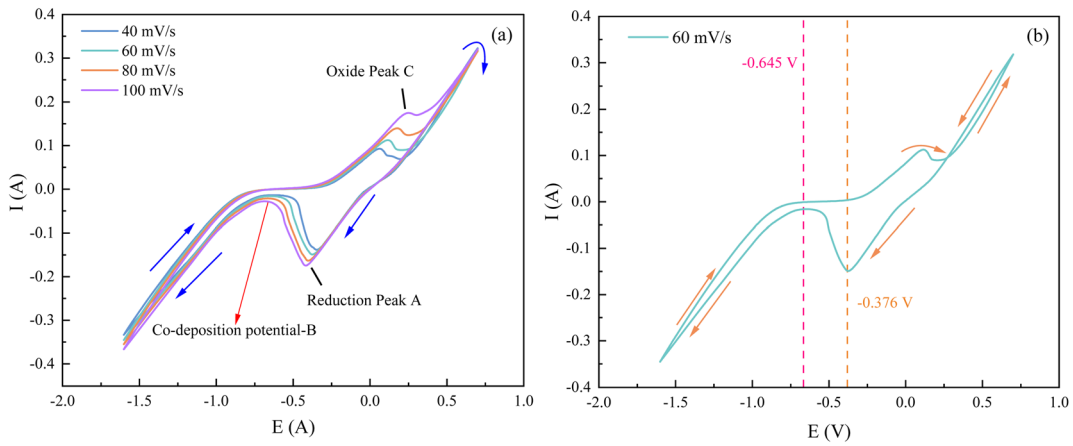

Fig. 9 (a) Cyclic voltammetry at different sweep speeds for Co–Ni–Ce; (b) 60 mV s^{-1} of Co–Ni–Ce.

Table 3 Calculated data related to the CV curve at any four points to the right of reduction peak (A and B)

	I_p/mA	I/mA	E/V	$\lg[\lvert(I_p - I)/I\rvert]$
−0.376 V	−145.56	−134.16	−0.2783	−1.0707
	−145.56	−135.28	−0.2807	−1.1194
	−145.56	−136.38	−0.2832	−1.1719
	−145.56	−137.45	−0.2856	−1.2291
−0.645 V	−15.994	−16.028	−0.654	−2.6725
	−15.994	−16.049	−0.657	−2.4636
	−15.994	−16.080	−0.659	−2.2695
	−15.994	−16.113	−0.662	−2.1284

It was calculated that Co^{2+} and Ni^{2+} first gained one electron each in the plating solution and combined with OH^- in the solution to form Co $(OH)_{ads}$ and Ni $(OH)_{ads}$, while Ce^{3+} combined with OH^- directly to form Ce $(OH)_{ads}$ adsorbed on the surface of Cu electrode. In Co–Ni–Ce alloy plating solutions, Ce cannot be deposited alone.[24] Instead, Co^+–Ni^+ induced formation of Ce metal is required.[24] The reduction of Ce^{3+} in aqueous solution at the Cu electrode was calculated to be a one-step, three-electron process, which can be represented by the following electrode reaction:

$$Co^{2+} + OH^- + e^- \rightarrow Co(OH)_{ads} \text{ and } Ni^{2+} + OH^- + e^- \rightarrow Ni(OH)_{ads}$$

$$Co(OH)_{ads} + Ni(OH)_{ads} \rightarrow Co(OH)_{ads} - Ni(OH)_{ads}$$

$$Ce(OH)_{ads}^{2-} + 3e^- \xrightarrow{Co(OH)_{ads}-Ni(OH)_{ads}+e^-+e^-} Co\text{-}Ni\text{-}Ce$$

To study the reversibility of the reaction, reduction control steps of Ce^{3+} on the copper electrode. The relevant data in the CV curves of Fig. 9(b) were fitted and calculated, and the relevant data are listed in Table 4 below.

As can be seen from Fig. 11(a), the relationship between the reduction peak potential (E_{pc}) and the $\ln \nu$ is line, indicating

Table 4 Sweep speed and peak potential, peak current correlation data presentation

ν/(V s^{-1})	0.040	0.060	0.080	0.100
$\ln \nu$/ln(V s^{-1})	−3.219	−2.813	−2.526	−2.303
$\nu^{1/2}$/(V s^{-1})$^{1/2}$	0.200	0.245	0.283	0.316
E_{pc}/V	−0.630	−0.645	−0.664	−0.676
$-I_{pc}$/A	0.003405	0.00410	0.005315	0.00650
$E_{p/2}$/V	−0.042	−0.037	−0.039	−0.044
ΔE_p	0.691	0.76	0.84	0.911
$\lvert E_{pc} - E_{p/2}\rvert$/V	0.588	0.608	0.625	0.640

that the reduction process of Ce^{3+} in the system plating solution is irreversible.[20] The irreversibility in the reduction process of Ce^{3+} is further demonstrated by the increase in the value of the ΔE_p with the ν in Table 4. To further determine the steps controlling the redox reactions of Ce^{3+}, the relationships between the peak currents I_{pc} and $\nu^{1/2}$ were investigated. The cathodic peak potential E_{pc} and half peak potential $E_{pc/2}$ satisfied the following equation:[25]

$$\left|E_{pc} - E_{pc/2}\right| = \frac{1.857RT}{\alpha nF} \quad (3)$$

The Nernst equation and CV tests allowed us to determine various parameters during the reduction of Ce^{3+} on the Cu plate, including the cathodic peak potential (E_{pc}) and half peak potential ($E_{pc/2}$) in volts, the charge transfer coefficient (α), and the number of transferred electrons (n). We substituted the respective values into eqn (3), and the mean value of α was calculated to be 0.0260 (Fig. 12).

The correlation coefficients of the linear fits of the peak currents I_{pc} with respect to $v_{1/2}$ are 0.934, respectively. The redox reaction of Ce^{3+} is controlled by diffusion, and the diffusion coefficient of Ce^{3+} can be derived from the Berzins–Delahay equation.[26,27]

$$I_{pc} = 0.496nFSC_0\left(\frac{\alpha nvFD_{Ce^{3+}}}{RT}\right)^{\frac{1}{2}} \quad (4)$$

where I_{pc} is the cathode peak current, n is the number of transferred electrons, S is the area of the working electrode/cm^2, C_0 is the

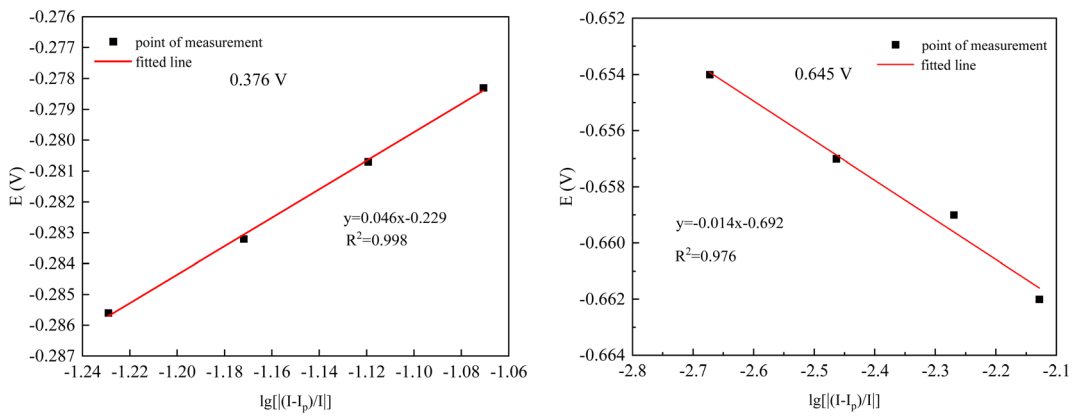

Fig. 10 Fitted datas from Table 3.

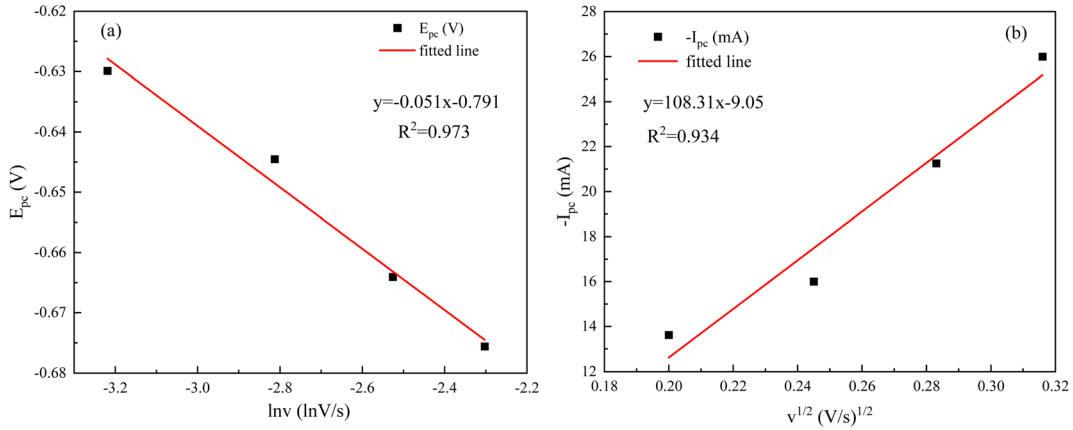

Fig. 11 Plot of sweep speed *versus*: (a) peak potential; (b) peak current.

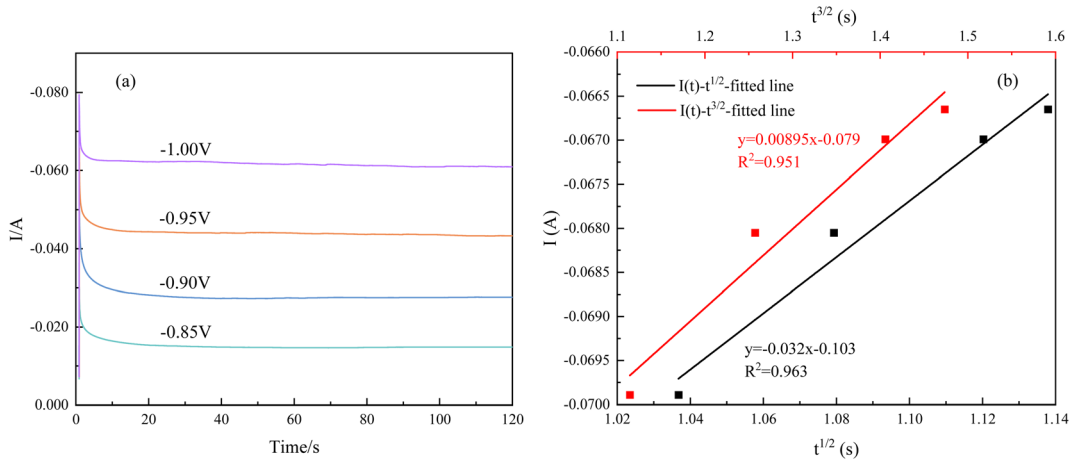

Fig. 12 (a) Chronoamperometric curves; (b) straight lines fitted to the nucleation method.

concentration of Ce^{3+}/mol L^{-1}, v is the sweeping velocity/mV s^{-1}, and $D_{Ce^{3+}}$is the diffusion coefficient of Ce^{3+}/cm^2 s^{-1}. The diffusion coefficient $D_{Ce^{3+}} = 8.23 \times 10^{-6}$ cm^2 s^{-1} of Ce^{3+} was obtained by taking the known data $I_{pc}/v^{1/2} = 108.31$ mA $s^{1/2}$ $mV^{-1/2}$, $n = 3$, $F =$ 96 500 C mol^{-1}, $R = 8.314$ J (mol K)$^{-1}$, $T = 298$ K, $\alpha = 0.0260$, $S = 2$ cm^2, and $C_0 = 0.054$ and by inserting these into the formula.

3.3.2 Chronoamperometric analysis. Upon application of various step potentials, the initial increment in current is observed, owing to the charging effect of the bilayer. Following this, there is a gradual reduction in current over time due to the migration effect of Ce^{3+} towards the cathode. The current eventually attains a stable state, signifying the onset of crystal growth and nucleation during this phase.[23] In an aqueous solution, the ion concentration is considerably greater compared to that on the cathode surface, giving rise to concentration polarization at the electrode surface. Eventually, a state of equilibrium is reached between the two regions, causing the current to remain unchanged.[24]

Instantaneous nucleation and continuous nucleation equations can be fitted from four different points arbitrarily taken from the rising portion of the different timing current curves in Fig. 11.[25]

Instantaneous nucleation:

$$I(t) = ZFN\pi(2D_{Ce^{3+}}C_0)^{\frac{3}{2}}M^{\frac{1}{2}}\rho^{-\frac{1}{2}}t^{\frac{1}{2}} \quad (5)$$

$$I(t) = kt^{\frac{1}{2}} + b_1 \quad (6)$$

Continuous nucleation:

$$I(t) = \frac{2}{3}ZFK_nN\pi(2D_{Ce^{3+}}C_0)^{\frac{3}{2}}M^{\frac{1}{2}}\rho^{-\frac{1}{2}}t^{\frac{3}{2}} \quad (7)$$

$$I(t) = kt^{\frac{3}{2}} + b_2 \quad (8)$$

In the above equations, $I(t)$- electron current corresponding to time/mA; Z-valence; F = 96 500 C mol^{-1}; N-the nucleation number density/cm^{-2}; $D_{Mo^{6+}}$-diffusion coefficient/cm^2 s^{-1}; C_0-concentration of Ce^{3+}/mol L^{-1}; M-molar mass/g mol^{-1}; ρ-density/g cm^{-3}; K_n-nucleation rate constant/cm^{-2} s^{-1}; t-time/s; and $\pi = 3.14$. Fig. 10 shows that the fitting degree of $I(t)$-$t^{1/2}$ is better than the fitting degree of $I(t)$-$t^{3/2}$ at any potential, which

indicates that the nucleation mechanism of Ce^{3+} on Cu plate is instantaneous nucleation.[24]

4 Conclusions

The following conclusions can be drawn from the study of the preparation of the Co–Ni–Ce/TiC alloy coating:

(1) XRD tests of Co–Ni–Ce/TiC coatings revealed that the addition of Ce affects the grain growth direction of Co–Ni alloys which would cause it to develop more towards the (200) crystal plane, and the addition of TiC would equalize this effect. SEM characterization confirmed that the introduction of Ce and TiC helps refine the grains and improve the surface quality of the alloy coatings. Furthermore, friction and wear tests demonstrated that the TiC nanoparticles play a lubricating role.

(2) The hardness of the Co–Ni–Ce/TiC alloy coatings prepared by double pulse deposition using aminosulfonic acid reaches 580.71 HV0.2, which is significantly higher than that of the Cu substrate and the Co–Ni coatings. Moreover, the wear rate of the Co–Ni–Ce/TiC alloy coating is 1.06×10^{-5} g m^{-1}, which is 5 times lower than that of the copper substrate, providing effective substrate protection.

(3) Cyclic voltammetry tests showed that the introduction of Ce^{3+} and TiC negatively shifts the co-deposition potential. The reduction reactions of Co^{2+} and Ni^{2+} are two-step, two-electron irreversible reactions, while the reduction reaction of Ce^{3+} is a one-step, three-electron process. The deposition of Ce^{3+} follows a diffusion-controlled, transient nucleation process, with a diffusion coefficient of 8.23×10^{-6} cm^2 s^{-1}.

Conflicts of interest

All authors disclosed no relevant relationships.

Acknowledgements

Supported by National Nature Science Foundation of China (52374352) and Open Project Fund of Provincial Key Laboratory of Metallurgical Engineering, Liaoning University of Science and Technology (2023KFKT-10). Supported by the Graduate science and Technology Innovation Program of University of Science and Technology Liaoning and Key Research (LKDYC202321). Supported by Liaoning Provincial Department of Education Key Public Relations Project (JYTZD2023091). Fig. 1 is Created with **https://www.biorender.com** (UV26IAQUHC).

References

1 S. Chen, J. Liang, C. Liu, *et al.*, Preparation of a novel Ni/Co-based alloy gradient coating on surface of the crystallizer copper alloy by laser, *Appl. Surf. Sci.*, 2011, **258**(4), 1443–1450.
2 X. Yang, X. Lu, W. Zhang, *et al.*, Preparation and application of nano-Ni–Co alloy, *J. Nanopart. Res.*, 2023, **25**(7), 152.
3 R. M. A. Radadi and M. A. M. Ibrahim, Nickel-cobalt alloy coatings prepared by electrodeposition Part II: Morphology, structure, microhardness, and electrochemical studies, *Korean J. Chem. Eng.*, 2021, **38**, 152–162.
4 Y. Chen, H. Yang, H. Feng, *et al.*, Electrodeposition and corrosion performance of Ni-Co alloys with different cobalt contents, *Mater. Today Commun.*, 2023, **35**, 106058.
5 S. Tebbakh, L. Mentar, Y. Messaoudi, *et al.*, Effect of cobalt content on electrodeposition and properties of Co–Ni alloy thin films, *Inorg. Nano-Met. Chem.*, 2021, **51**(12), 1796–1802.
6 E. Gao, G. Wei, B. Yan, *et al.*, Effect of Graphene Content on the Micromorphology, Microhardness and Micro Frictional Resistance of Co-Ni-Graphene Composite Coating, *Mater. Sci. Forum*, 2021, **1035**, 608–614.
7 X. Fu, Q. Wang, J. Lin, *et al.*, Effect of Ce (SO4) (2) Concentration on Properties of Ni-W-Ce Alloy Coating Prepared by Jet-electrodeposition, *Rare Met. Mater. Eng.*, 2020, **49**(9), 2948–2955.
8 X. Zhang, H. Chen, X. Li, *et al.*, Effect of Rare Earth on the Microstructure and Performance of Electrodeposited Ni-W Coatings, *Rare Met. Mater. Eng.*, 2016, **45**(10), 2605–2608.
9 B. Li, J. Su, J. Li, *et al.*, Comparison of the Effect of Mechanical and Ultrasonic Agitation on the Properties of Electrodeposited Ni-Co/ZrO2 Composite Coatings, *Metals*, 2023, **13**(3), 478.
10 H. Wang, X. Mao, T. Shen, *et al.*, Effect of Nano-TiC Particles on Microstructure and Properties of Ni-TiC Composite Coatings, *J. Mater. Eng.*, 2017, **45**(1), 52–57.
11 F. Cheng, Z. Cao and Z. Wen, *et, al.*, Surface of AISI 430 stainless steel Pulsed electrodeposition of Co-Ni alloys, *Mater. Prot.*, 2015, **48**(07), 11–14.
12 H. Tian, Fundamental Research on Manufacturing Technology and Properties of Ni-Based Nano-Composite Coatings by Electrophoretic-Electrochemical Deposition, PhD thesis, Nanjing University of Aeronautics and Astronautics, 2008.
13 W. Jia, Study of Electroless Co-ni-P Alloy Films with Rare Earth Element Cerium Addition, PhD thesis, Hefei University of Technology, 2007.
14 X. Ren, S. Wu and R. Jiang, *et, al.*, Preparation and structural characterization of Ni-nano-TiC composite coating under pulse condition, *Ordnance Mater. Sci. Eng.*, 2019, **42**(05), 74–77.
15 L. Burzyńska and E. Rudnik, The influence of electrolysis parameters on the composition and morphology of Co–Ni alloys, *Hydrometallurgy*, 2000, **54**(2–3), 133–149.
16 A. N. Correia and S. A. S. Machado, Electrodeposition and characterisation of thin layers of Ni-Co alloys obtained from dilute chloride baths, *Electrochim. Acta*, 2000, **45**(11), 1733–1740.
17 P. Zhou, W. Li, Y. Li, *et al.*, Fabrication and corrosion performances of pure Ni and Ni-based coatings containing rare earth element Ce and graphene by reverse pulse electrodeposition, *J. Electrochem. Soc.*, 2017, **164**(2), D75.
18 J. Zhou, X. Meng, R. Zhang, *et al.*, Progress on electrodeposition of rare earth metals and their alloys, *Electrocatalysis*, 2021, 1–13.
19 S. You, C. Jiang, L. Wang, *et al.*, Effect of CeO2 nanoparticles on the microstructure and properties of the NiCo-CeO2 composite coatings, *Vacuum*, 2022, **196**, 110765.

20 H. Kang, J. Li, C. Zhang, *et al.*, Study of the electrochemical recovery of cobalt from spent cemented carbide, *RSC Adv.*, 2020, **10**(37), 22036–22042.
21 H. Xing, J. Li, X. Hu, *et al.*, Repair of soft magnetic properties of wasted silicon steel and Co7Fe3 alloy deposition mechanism, *RSC Adv.*, 2023, **13**(47), 33525–33532.
22 X. Zhou, Y. Shen, H. Jin, *et al.*, Microstructure and depositional mechanism of Ni–P coatings with nano-ceria particles by pulse electrodeposition, *Trans. Nonferrous Met. Soc. China*, 2012, **22**(8), 1981–1988.
23 D. Escorcia-Díaz, S. García-Mora, L. Rendón-Castrillón, *et al.*, Advancements in Nanoparticle Deposition Techniques for Diverse Substrates: A Review, *Nanomaterials*, 2023, **13**(18), 2586.
24 H. Xing, J. Li, X. Hu, *et al.*, Mechanism study of composite co-deposited Cu/Co-Mo corrosion-resistant coating on 6061 Al alloy, *Surf. Coat. Technol.*, 2024, **476**, 130202.
25 Z. Hou, J. Li, X. Wang, *et al.*, Effect of Tin Ion on Electrodeposition Behavior of Indium, *Electrochemistry*, 2022, **90**(8), 087007.
26 T. Berzins and P. Delahay, Kinetics of fast electrode reactions, *J. Am. Chem. Soc.*, 1955, **77**(24), 6448–6453.
27 E. Gomez, E. Pellicer and E. Valles, Detection and characterization of molybdenum oxides formed during the initial stages of cobalt–molybdenum electrodeposition, *J. Appl. Electrochem.*, 2003, **33**, 245–252.